

L-PR: Exploiting LiDAR Fiducial Marker for Unordered Low Overlap Multiview Point Cloud Registration

Yibo Liu, Jinjun Shan, Amaldev Haridevan, Shuo Zhang

Abstract—Point cloud registration is a prerequisite for many applications in computer vision and robotics. Most existing methods focus on pairwise registration of two point clouds with high overlap. Although there have been some methods for low overlap cases, they struggle in degraded scenarios. This paper introduces a novel framework dubbed L-PR, designed to register unordered low overlap multiview point clouds leveraging LiDAR fiducial markers. We refer to them as LiDAR fiducial markers, but they are the same as the popular AprilTag and ArUco markers—thin sheets of paper that do not affect the 3D geometry of the environment. We first propose an improved adaptive threshold marker detection method to provide robust detection results when the viewpoints among point clouds change dramatically. Then, we formulate the unordered multiview point cloud registration problem as a maximum a-posteriori (MAP) problem and develop a framework consisting of two levels of graphs to address it. The first-level graph, constructed as a weighted graph, is designed to efficiently and optimally infer initial values of scan poses from the unordered set. The second-level graph is constructed as a factor graph. By globally optimizing the variables on the graph, including scan poses, marker poses, and marker corner positions, we tackle the MAP problem. We conduct both qualitative and quantitative experiments to demonstrate that the proposed method surpasses previous state-of-the-art (SOTA) methods and to showcase that L-PR can serve as a low-cost and efficient tool for 3D asset collection and training data collection. In particular, we collect a new dataset named Livox-3DMatch using L-PR and incorporate it into the training of the SOTA learning-based method, SGHR, which brings evident improvements for SGHR on various benchmarks. We release the open-source code implementation and datasets at <https://github.com/yorklyb/L-PR>.

Index Terms—LiDAR Fiducial Marker; Multiview Point Cloud; Low Overlap; Registration; Dataset.

I. INTRODUCTION

POINT cloud registration is a fundamental need in computer vision [1], [2] and robotics [3], [4], [5]. Most existing point registration methods [3], [6] focus on pairwise registration of two point clouds with high overlap, which are not robust in practical applications [2]. Some recent learning-based research proposes multiview registration methods [1], [7] and studies low overlap cases [2], [1]. Despite their promising performance on benchmarks, the generalization of learning-based methods to unseen scenarios (*i.e.*, out-of-distribution cases of training data) remains problematic. Moreover, both geometry-based methods [3], [4], [5], [8] and learning-based methods [1], [2] rely on geometric features in the scenes to align point clouds. Hence, these methods struggle in degraded

This work was supported by NSERC Alliance Grant ALLRP 555847-20 and Mitacs Accelerate Grant IT26108. (Corresponding author: Jinjun Shan.)

Yibo Liu, Jinjun Shan, Amaldev Haridevan, and Shuo Zhang are with the Department of Earth and Space Science, Lassonde school of Engineering, York University, Toronto, Ontario, M3J1P3, Canada. email:{yorklyb,jjshan,amaldev,shuoy}@yorku.ca

scenes [9], such as those with repetitive structures and weak textures.

Reviewing the domain of 2D images, it is found that fiducial markers, such as AprilTag [10] and ArUco [11], have been widely used to tackle challenging situations, such as dramatic viewpoint changes (low overlap) between frames and textureless environments [12], [13], [14]. The visual fiducial markers have rich patterns that are robust for detection and matching, thanks to elaborately designed encoding-decoding algorithms [10], [11]. They pose as thin sheets of paper that can be attached to surfaces without disrupting the 3D environment. In contrast, fiducial objects developed for LiDARs, such as calibration boards [15], [16], [17], lack encoding-decoding pattern design and often take the form of large boards mounted on tripods, thus affecting the 3D environment. LiDARTag [18] is the first work to develop a fiducial marker system akin to AprilTag [10] for LiDARs. While its patterns are compatible with AprilTag, the marker itself is still an additional object placed on a tripod. Recently, the intensity image-based LiDAR fiducial marker system (IFM) [19] proposes to utilize intensity and range images to detect markers. Thus, IFM is compatible with popular visual fiducial markers [10], [11] and inherits the virtue of not affecting the 3D environment. However, the marker detection of IFM is not robust when the viewpoints change in a wide range [19], which hinders its application to in-the-wild multiview point cloud registration. Although the development of LiDAR fiducial markers [18], [19] has advanced, their applications are limited to calibration [20] and AR [19]. The utilization of LiDAR fiducial markers in multiview point cloud registration remains an open problem.

Furthermore, training data is crucial for the development of learning-based point cloud registration methods [2], [1], but collecting it is time-consuming and expensive. For instance, in previous dataset collections [6], [21], [22], external sensors such as cameras, IMUs, and GPS are employed to obtain ground truth poses among point clouds. This requires careful multi-sensor calibration and synchronization, which can be time-consuming and labor-intensive.

In this paper, we develop a novel framework, dubbed L-PR (see Fig. 1), to exploit LiDAR fiducial markers for unordered low overlap multiview point cloud registration. L-PR is a new solution for training data collection that only uses a LiDAR sensor. As seen, the LiDAR fiducial markers are thin sheets of board/paper attached to other surfaces without impacting the environment. Specifically, the LiDAR fiducial markers can be printed on paper using standard printers, offering a low-cost, easy-to-use, and reliable alternative compared to previous external sensors. Given an unordered set of low overlap point clouds, the proposed L-PR efficiently registers them in a global frame. To address the unstable marker detection of IFM [19]

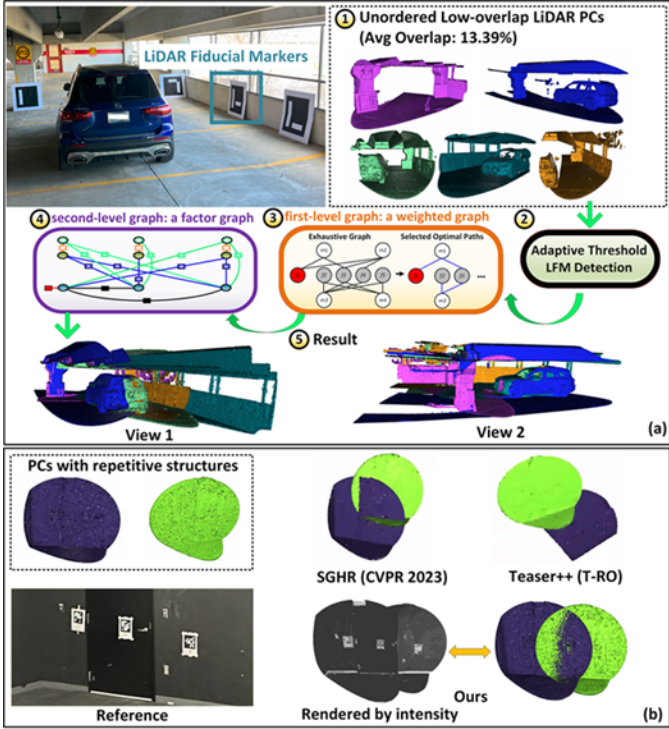


Fig. 1. (a): **Overview of L-PR.** (1) Given an unordered set of unaligned, low overlap 3D point clouds, we aim to register them into (5) a complete point cloud utilizing LiDAR fiducial markers (thin sheets of paper/board attached to other planes). This is achieved through the proposed (2) adaptive threshold marker detection method and the (3)(4) two-level graphs. The (3) first-level graph handles the unordered set of point clouds and calculates initial values. The (4) second-level graph registers the point clouds by finding the optimal solution to a maximum a-posteriori problem. (b): The proposed method is robust to degraded scenes, such as scenes with repetitive structures.

in the wild, we first develop an adaptive threshold marker detection method that is robust to viewpoint switching. Then, we formulate the multiview point cloud registration problem as a maximum a-posteriori (MAP) problem and develop two-level graphs to tackle it. The first-level graph, constructed as a weighted graph, is designed to efficiently process the unordered set of point clouds and calculate the initial values of poses among point clouds. In particular, the weights represent the pose estimation error of each marker observation, and we obtain the optimal solutions of initial values by finding the shortest path from an anchor scan to each non-anchor scan on the graph. Given the initial values, we design the second-level graph, a factor graph, to resolve the MAP problem by globally optimizing the poses of point clouds, markers, and positions of marker corners. We conduct both qualitative and quantitative experiments to demonstrate the superiority of the proposed method over competitors [1], [3], [14], [4] and to showcase the diverse applications of L-PR, including 3D asset collection, training data collection, reconstruction of a degraded scene, localization in a GPS-denied environment, and 3D map merging. We release the code implementation and datasets at <https://github.com/yorklyb/L-PR>.

The **contributions** of this work are as follows:

- We design a novel framework, named **L-PR**, for unordered low overlap multiview point cloud registration leveraging LiDAR fiducial markers. L-PR can serve as an

efficient and reliable tool to collect 3D assets and training data for learning-based methods.

- We collect a new training dataset called **Livox-3DMatch** using the proposed L-PR. Livox-3DMatch augments the original 3DMatch training data [6] from 14,400 pairs to 17,700 pairs (a **22.91%** increase). By training on this augmented dataset, the performance of the SOTA learning-based method SGHR [1] is improved by **2.90%** on 3DMatch [6], **4.29%** on ETH [21], and **22.72%** (translation) / **11.19%** (rotation) on ScanNet [22].
- We develop an improved LiDAR fiducial marker detection algorithm which is robust to viewpoint changes.

II. RELATED WORKS

LiDAR Fiducial Markers. Given the success of Structure from Motion [12], [14] and visual Simultaneous Localization and Mapping (SLAM) [13], [23] approaches based on visual fiducial markers [10], [11], why do we still need to exploit LiDAR and LiDAR fiducial markers? There are three reasons. (1) Unlike image-based fiducial marker detection, which is sensitive to ambient light, LiDAR fiducial marker detection is robust to unideal illumination conditions [18], [19], such as purely dark or overexposed environments. (2) Unlike image-based fiducial marker detection, which suffers from rotational ambiguity [12], [14], [13] and requires abandoning ambiguous measurements, LiDAR fiducial marker pose estimation is not affected by rotational ambiguity [18], [19] and each marker observation can be utilized. (3) Data captured by LiDARs is irreplaceable by data acquired from cameras due to the unique modality of LiDAR point cloud [24].

Most LiDAR fiducial objects [15], [16], [17] are designed for calibration purposes. Fig. 2(a) shows a typical calibration board, a thick board with holes and/or regions covered by high-intensity materials. A calibration board is commonly placed on a tripod for spatial distinction, making it an additional 3D object that affects the environment. Moreover, while a calibration board can provide fiducials (holes, corners, and high-intensity regions) and it is feasible to assign specific indexes to the fiducials, a calibration board is fundamentally different from fiducial marker systems [10], [11]. The core of fiducial marker systems [10], [11] lies in the elaborately designed encoding-decoding algorithms, leveraging which various complex patterns are generated as depicted in Fig. 2(b). In addition to supporting a larger number of unique IDs, the patterns of fiducial markers are robust against false positive/negative issues. Recently, utilizing the encoding-decoding algorithm of AprilTag 3 [10], the first fiducial marker system for LiDARs, named LiDARTag, is introduced in [18]. Unfortunately, as presented in Fig. 2(c), a LiDARTag is still an additional 3D object impacting the 3D environment. This is undesirable when collecting training data for learning-based point cloud registration methods. IFM [19] develops a LiDAR fiducial marker system that can be integrated with various visual fiducial marker systems [10], [11]. Furthermore, as seen in Fig. 2(d), the usage/placement of IFM is as convenient as the visual fiducial marker. Nevertheless, the marker detection of IFM is unstable when the viewpoints change dramatically

among scans due to the use of a constant threshold to process the intensity image [19]. We develop an improved adaptive threshold marker detection method to address this problem because robust marker detection is the prerequisite for exploiting markers in point cloud registration.

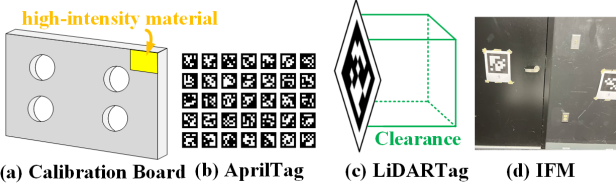


Fig. 2. (a) Typical calibration board: forms a thick board with holes and/or regions with high-intensity materials. It impacts the 3D environment and does not support patterns generated by an encoding-decoding algorithm. (b) AprilTag [10]: has rich patterns generated from the encoding-decoding algorithm and is thus robust to false positives/negatives. It has no effect on the 3D environment but is designed for cameras. (c) LiDARTag [18]: has patterns compatible with AprilTag [10] but still forms an additional 3D object. (d) IFM [19]: has patterns compatible with AprilTag [10] and ArUco [11]. It has no impact on the 3D environment.

Point Cloud Registration. Geometry-based point cloud registration methods, such as variants of iterative closest point methods [4], [5], RANSAC [8], and Teaser++ [3], mainly focus on designing efficient and robust algorithms for describing geometry and extracting geometric features (*e.g.*, points, lines, and surfaces/normals) to find correspondence between point clouds and align them. In learning-based point cloud registration methods like Predator [2] and SGHR [1], neural networks are designed to learn features representing the geometry [25], [26], [27], [7], [6], and then learn to utilize these features for registering the point clouds. While these methods demonstrate remarkable performance on benchmarks [6], [21], [22], they still face challenges in handling degraded scenes, such as repetitive structures and textureless environments. Moreover, most existing methods [28], [4], [5], [27], [6] only apply to high overlap scenarios. Despite the existence of some research [1], [2] on low overlap cases, their generalization to unseen scenes is limited. Inspired by the utilization of visual fiducial markers in camera-based applications [12], [14], [13], [23] to handle degraded scenes and low overlap cases, we propose exploiting LiDAR fiducial markers to enhance multiview point cloud registration.

III. METHODOLOGY

A. Adaptive Threshold LiDAR Fiducial Marker Detection

Preliminaries. Given a 3D point cloud, IFM [19] generates a 2D intensity image by mapping each 3D point to a pixel on an image plane:

$$u = \lceil \frac{\theta}{\alpha_a} \rceil + u_o, \quad v = \lceil \frac{\phi}{\alpha_i} \rceil + v_o, \quad (1)$$

where $[u, v]^T$ denote the image coordinates of the projected pixel. $[\theta, \phi, r]^T$ denote the spherical coordinates of the 3D point. α_a and α_i represent the angular resolutions in u (azimuth) and v (inclination) directions, respectively. u_o and v_o are the offsets. The pixel value $I(u, v)$ is decided by the corresponding intensity value through the color map. The

ranging information is also saved for each pixel. In the real world, the intensity values of the same surface of an object could vary, leading to noise in the rendered image. To denoise the intensity image, each pixel is binarized with a threshold λ . In [19], λ is set as a constant. Then, the embedded 2D marker detector [10], [11] is applied to localize the fiducials on the binarized image. Using the ranging information, the detected 2D fiducials are projected back into 3D space via the reverse of Eq. (1) and become 3D fiducials.

Adaptive Threshold Method. As aforementioned, binarization is applied to the raw intensity image due to the imaging noise (see the zoomed view of Fig. 3). As seen, the effect is determined by the threshold λ . In [19], it is found that λ can be selected as a constant if the viewpoint does not change drastically. However, with significant changes in the scene, the value of λ needs adjustment. As an example, consider the case shown in Fig. 3, where three markers are placed. Markers ID 1 and 4 are detectable when $\lambda=13$, while marker ID 3 is detectable when $\lambda=70$. Thus, $\lambda=13$ and $\lambda=70$ are the optimal thresholds compared to other values for markers ID 1 and 4 and marker ID 3, respectively, denoted by λ^* .

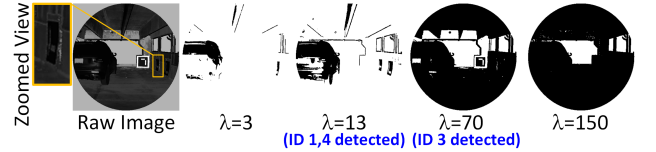


Fig. 3. The raw intensity image binarized with different threshold values.

Therefore, unless an appropriate λ is carefully selected for each scan, and even for each marker, the LiDAR fiducial marker detection will fail. Unlike [19], which determines λ^* based on experience or experimentation, we develop an algorithm to automatically seek λ^* . Given that our focus is on marker detection rather than image denoising, we design **Algorithm 1** that utilizes the detection result as the feedback to search for λ^* automatically. In particular, the core of the algorithm is to maximize the length of a memory queue for saving detected markers (denoted by Q) by gradually increasing λ . Namely, we aim to detect as many markers as possible by finding the optimal threshold for each marker in the scene. After applying **Algorithm 1**, the 2D fiducials located on the image binarized with λ^* are projected into 3D fiducials using the subsequent steps of IFM [19]. Our algorithm addresses the problem of a constant threshold being inapplicable to all scans and markers, especially when LiDAR moves in the wild and scenes undergo significant changes.

B. Problem Formulation

In this section, we introduce the problem formulation. Suppose that the marker size is l . In the marker coordinate system $\{M\}_j$, we know that the 3D coordinates of the four corners of the j -th marker, ${}^j\mathbf{p}^{j,1}, {}^j\mathbf{p}^{j,2}, {}^j\mathbf{p}^{j,3}$, and ${}^j\mathbf{p}^{j,4}$, are $[-l/2, -l/2, 0]^T, [l/2, -l/2, 0]^T, [l/2, l/2, 0]^T$, and $[-l/2, l/2, 0]^T$, respectively. LiDAR fiducial marker detection returns the 3D coordinates of the corners expressed in $\{F\}_i$ (the local coordinate system of the i -th scan f_i) [19]. Thus,

Algorithm 1: Search for the optimal threshold, λ^* .

Input: Raw intensity image, \mathbf{I}
Output: The optimal threshold, λ^* .

Initialize parameters: Search scope, S . step size, δ . queue for saving detected markers, $Q = []$. length of Q , $Q_l = 0$. temporary queue, $Q_{temp} = []$, length of $Q_{temp} = []$, $Q_{temp,l} = 0$. the optimal threshold, $\lambda^* = 0$. search step, $i = 0$.
Define the binarization operation as $\Psi(\mathbf{I}, \lambda)$.Define the marker detector operation as $\Gamma(\mathbf{I})$.
while $i < S$ **do**

$$\begin{aligned} \lambda &= \delta \times i \\ \mathbf{I} &= \Psi(\mathbf{I}, \lambda) \\ \Gamma(\mathbf{I}) &\rightarrow Q_{temp} \\ \text{if } Q_{temp,l} \geq Q_l \text{ then} \\ \quad \text{for marker in } Q_{temp} \text{ do} \\ \quad \quad \text{if marker not in } Q \text{ then} \\ \quad \quad \quad \text{append marker to } Q \\ \quad \lambda^* &= \lambda \\ i &= i + 1 \end{aligned}$$
Return the image binarized with λ^* and Q .

the 6-DOF transmission from $\{M\}_j$ to $\{F\}_i$, denoted as \mathbf{T}_i^j , can be found by solving the following least square problem:

$$\mathbf{T}_i^{j,*} = \arg \min_{\mathbf{T}_i^j} \sum_{s=1}^4 \left\| \mathbf{T}_i^j \cdot {}^j \mathbf{p}^{j,s} - {}_i \mathbf{p}^{j,s} \right\|^2. \quad (2)$$

The Singular Value Decomposition (SVD) method [29] is employed to compute $\mathbf{T}_i^{j,*}$. We denote the set of measurements, including (1) the corner positions *w.r.t.* $\{M\}_j$, (2) the corner positions *w.r.t.* $\{F\}_i$, and (3) the marker poses *w.r.t.* $\{F\}_i$, as \mathcal{Z} . To register the multiview point clouds, we need to find a globally consistent pose for every scan so that the point clouds can be transformed into a complete point cloud in the global coordinate system $\{G\}$. To achieve this objective, we consider the following variables in this work: (1) the poses of point clouds *w.r.t.* $\{G\}$, (2) the poses of markers *w.r.t.* $\{G\}$, and (3) the marker corner positions *w.r.t.* $\{G\}$. We specify the set of variables as Θ . Finally, a maximum a-posteriori (MAP) inference problem is formulated: given the measurements, \mathcal{Z} , the goal is to find the optimal variable set Θ^* that maximizes the posterior probability $P(\Theta | \mathcal{Z})$:

$$\Theta^* = \arg \max_{\Theta} P(\Theta | \mathcal{Z}). \quad (3)$$

In the following, we design a framework consisting of two-level graphs to resolve this MAP problem. Inspired by the coarse-to-fine pipeline of SGHR [1], we develop a first-level graph to efficiently and exhaustively determine the relative poses among point clouds, and a second-level graph to globally optimize the variables.

C. First-level Graph

As aforementioned, the variables in Θ to be optimized cannot be directly obtained through the measurements in \mathcal{Z} . Moreover, deriving the initial values of the variables requires both

efficiency and accuracy, given that the input is an unordered set of low overlap point clouds. To address this challenge, we design the first-level graph. First, we consider computing the relative pose between two point clouds. Suppose the j -th marker appears in the scenes of two scans f_i and f_m , \mathbf{T}_i^j and \mathbf{T}_m^j can be calculated using Eq. (2). Consequently, the relative pose between f_i and f_m , denoted as $\mathbf{T}_{i,m}$, is available from

$$\mathbf{T}_{i,m} = (\mathbf{T}_i^j)^{-1} \mathbf{T}_m^j, \quad (4)$$

where $(\mathbf{T}_i^j)^{-1}$ indicates the inverse of \mathbf{T}_i^j . $(\mathbf{T}_i^j)^{-1}$ indicates the pose that transforms 3D points from $\{F\}_i$ to $\{M\}_j$. Although the method introduced in Eq. (4) is straightforward, it cannot be directly applied because the input in this work is an unordered set of point clouds that do not follow a temporal or spatial sequence. Specifically, for scans with no shared marker observations, their relative pose has to be calculated through pose propagation among other scans. However, multiple alternative paths could exist. Even for scans that share marker observations, there could be more than one overlapped marker. Hence, to accurately and efficiently estimate relative poses among scans, it is necessary to design an algorithm to determine which scans and markers to apply Eq. (4).

Specifically, our objective is to infer the relative poses with the highest possible accuracy using only the necessary low-dimensional information through a simple process. Thus, we construct the first-level graph as a weighted graph. The construction of this graph is as follows. When processing the point clouds with the proposed adaptive threshold method one by one, if a marker is detected in a point cloud, we add the corresponding scan node and marker node to the graph along with a weighted edge. The edge weight is the pose estimation point-to-point error e_{pp} :

$$e_{pp} = \sum_{s=1}^4 \left\| \mathbf{T}_i^{j,*} \cdot {}^j \mathbf{p}^{j,s} - {}_i \mathbf{p}^{j,s} \right\|^2. \quad (5)$$

Eq. (5) indicates the substitution of the result given by SVD back into the right side of Eq. (2). $e_{pp} \in \mathbb{R}^+$ is employed as the metric to evaluate the quality of pose estimation of the marker in the corresponding point cloud. We define the first scan as the anchor scan. The local coordinate system of the anchor scan is set as the global coordinate system. Namely, $\{F\}_1 = \{G\}$. We only consider the relative poses between the anchor scan and each non-anchor scan. Although there could be multiple paths from the given scan to the anchor scan (see Fig. 4), we have already saved the information on pose estimation quality by constructing the first-level graph as a weighted graph.

Therefore, we adopt Dijkstra's algorithm [30] to obtain the shortest path. Then, we compute the relative pose along the shortest path iteratively using Eq. (4). Given that the relative pose computation is achieved with the lowest accumulation of e_{pp} , the estimation result achieves the highest possible accuracy. Moreover, the search for the optimal path to propagate poses is based merely on the one-dimensional e_{pp} , without incorporating any 6-DOF poses or 3D locations.

In this way, the point cloud poses *w.r.t.* $\{G\}$ are obtained. Since the marker detection provides the marker poses and

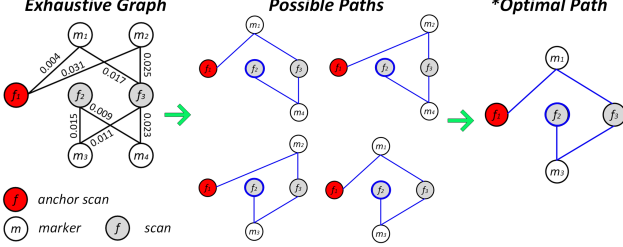


Fig. 4. An illustration of the first-level graph. In this simple case, as shown on the right side, four alternative paths exist from f_2 to the anchor scan (f_1). We employ Dijkstra's algorithm [30] to find the shortest path.

the 3D positions of marker corners *w.r.t.* the local coordinate system of corresponding scan, we can derive the initial values of the marker poses *w.r.t.* $\{G\}$ and the corner positions *w.r.t.* $\{G\}$ through the point cloud poses *w.r.t.* $\{G\}$.

D. Second-level Graph

In this section, we construct a factor graph to optimize the variables, ultimately addressing the MAP inference problem introduced in Eq. (3). Suppose that the j -th marker is detected in the i -th scan, the following nodes are added to the second graph. The variable nodes include \mathbf{T}^j (6-DOF pose of the j -th marker *w.r.t.* $\{G\}$), \mathbf{T}_i (6-DOF pose of the i -th scan *w.r.t.* $\{G\}$), and $\{\mathbf{p}^{j,1}, \mathbf{p}^{j,2}, \mathbf{p}^{j,3}, \mathbf{p}^{j,4}\}$ (3D coordinates of the corners of the j -th marker *w.r.t.* $\{G\}$). The factor nodes include \mathbf{T}_i^j (6-DOF pose of the j -th marker *w.r.t.* $\{F\}_i$), $\{\mathbf{p}^{j,1}, \mathbf{p}^{j,2}, \mathbf{p}^{j,3}, \mathbf{p}^{j,4}\}$ (3D coordinates of the corners of the j -th marker *w.r.t.* $\{M\}_j$), and $\{\mathbf{p}^{j,1}, \mathbf{p}^{j,2}, \mathbf{p}^{j,3}, \mathbf{p}^{j,4}\}$ (3D coordinates of the corners of the j -th marker *w.r.t.* $\{F\}_i$). Note that by adding variables representing the 3D coordinates of the corners, we can also optimize the fiducial localization results at this stage. For clarity, the first stage in Fig. 5 shows the added nodes and edges when a marker is detected in a scan. The graph becomes the one depicted in the second stage of Fig. 5 after integrating all the marker detection results.

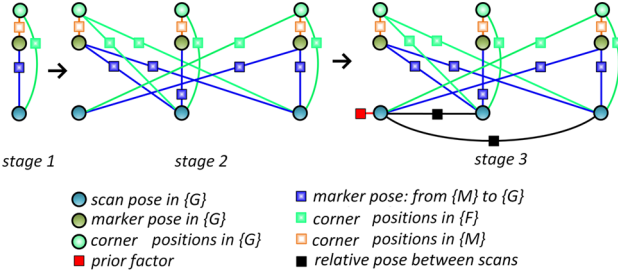


Fig. 5. The procedures for formulating the second graph. The variable nodes are represented by circles and the factor nodes are represented by squares.

Subsequently, we add a prior factor that connects to the first (anchor) point cloud pose node since we set $\{F\}_1$ as $\{G\}$. Finally, we add factor nodes representing the relative poses between the anchor scan and each non-anchor scan. Up to this point, the factor graph is completed, as shown in Stage 3 of

Fig. 5. Following [31], [32], this indicates that the factorization of the posterior probability $P(\Theta | \mathcal{Z})$ has been defined:

$$P(\Theta | \mathcal{Z}) = \prod_k P^{(k)}(\Theta), \quad (6)$$

where $P^{(k)}$ are the factors in the second graph and we follow the standard pipeline [31] to model them as Gaussians:

$$P^{(k)}(\Theta) \propto \exp\left(-\frac{1}{2} \|h_k(\Theta) \ominus z_k\|_{\Sigma_k}^2\right), \quad (7)$$

where $h_k(\Theta)$ is the measurement function and z_k is a measurement. $\|e\|_{\Sigma}^2 \triangleq e^T \Sigma^{-1} e$ denotes the squared Mahalanobis distance with Σ being the covariance matrix. Following [23], if $z_k \in \mathbb{R}^{3 \times 1}$ is a 3D position, \ominus refers to straight subtraction for elements. If $z_k \in SE(3)$ is a 6-DOF pose, \ominus generates 6-dimensional Lie algebra coordinates:

$$\mathbf{T}_A \ominus \mathbf{T}_B = [\log(\text{Rot}(\mathbf{T}_B^{-1} \mathbf{T}_A))]_v^T, \text{Trans}(\mathbf{T}_B^{-1} \mathbf{T}_A)^T, \quad (8)$$

where for a $\mathbf{T} \in SE(3)$, $\text{Rot}(\mathbf{T})$ denotes the rotation matrix $\mathbf{R} \in SO(3)$ and $\text{Trans}(\mathbf{T})$ denotes translation vector $\mathbf{t} \in \mathbb{R}^{3 \times 1}$. $\log(\cdot)$ represents the matrix logarithm. \vee is the *vee* map operator that finds the unique vector $\xi \in \mathbb{R}^{3 \times 1}$ (Lie algebra coordinates) corresponding to a given skew-symmetric matrix $\log(\mathbf{R}) \in \mathbb{R}^{3 \times 3}$ [29], [23]. With the Gaussian modeling, the objective function in Eq. (6) is transformed into a least square problem by applying the negative logarithm:

$$\arg \min_{\Theta} (-\log \prod_k P^{(k)}(\Theta)) = \arg \min_{\Theta} \frac{1}{2} \sum_k \|h_k(\Theta) \ominus z_k\|_{\Sigma_k}^2. \quad (9)$$

We utilize the Levenberg-Marquardt algorithm [32] to solve this problem. The acquisition of initial values is introduced in Section III-C. The noise covariance matrices are determined by the quantitative experiments conducted in [19].

IV. LIVOX-3DMATCH DATASET

A common approach [1], [2] to evaluating a learning-based point cloud registration model is to train it on 3DMatch [6] and test it on various benchmarks, including 3DMatch [6], ETH [21], and ScanNet [22]. However, the 3DMatch benchmark is mainly constructed from RGB-D camera captures of indoor scenes [6]. In this work, we collect a new dataset named Livox-3DMatch to enrich the training data for learning-based methods. The enrichment contains two key components. Firstly, the sensor we adopt is a Livox MID-40 LiDAR, which has different sampling patterns compared to the RGB-D camera (see Fig. 6(a) and (b)). Thus, it adds point clouds with new features to the training data. Secondly, we selectively sampled some scenes that are absent or rare in 3DMatch, thereby enriching the scenes in the training data. For example, the valid depth range of an RGB-D camera is usually less than ten meters, making it unsuitable for sampling outdoor scenes. In contrast, we collect some outdoor scenes (see Fig. 6(c)) for Livox-3DMatch, considering that a LiDAR can sample objects a few hundred meters away. Moreover, we collect some challenging cases (see Fig. 6(d)) where the overlapping regions are mainly planes, which are rare in 3DMatch [6]. A more detailed introduction to the scenes in Livox-3DMatch is given in Sections V-B and V-C. In Section V-D, we demonstrate that

the proposed Livox-3DMatch can boost the performance of the SOTA learning-based method [1] on various benchmarks [6], [21], [22].

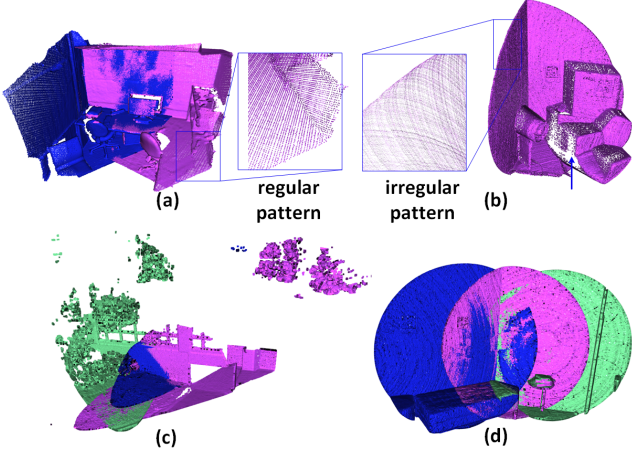


Fig. 6. Comparison of 3DMatch and Livox-3DMatch. (a): A random sample from 3DMatch. The point cloud sampled by an RGB-D camera has a regular pattern and less noise. (b): A random sample from Livox-3DMatch. The Livox LiDAR point cloud has an irregular pattern and more noise. (c): An example of an outdoor scene in Livox-3DMatch. (d): A selectively sampled challenging case in which the overlapping regions are mainly planes.

V. EXPERIMENTAL RESULTS

In this section, we report the experimental results of seven tests to demonstrate the effectiveness and applications of the proposed method from different perspectives.

A. Evaluation of the Adaptive Marker Detection Method

Data. We place the Livox MID-40 LiDAR and 69.2 cm \times 69.2 cm ArUco marker(s) in three different scenes, as shown in Fig. 7. The three scenes are: between groups of buildings, in open outdoor areas, and in large indoor parking lots. In each scene, we collect point clouds and test the proposed adaptive threshold method at different relative positions. **Results and Analysis.** Table I presents the results, where x and y indicate the relative position of the LiDAR in the marker (ID 4) coordinate system. Specifically, in scene Fig. 7(c), there are two markers (ID 4 and ID 1), so the column for λ^* contains two values. As seen in the table, λ^* varies significantly as the relative position changes, demonstrating the necessity of the proposed adaptive marker detection method. In addition, the results shown in Fig. 7(c) also illustrate the necessity of the memory queue design, considering that a single λ^* might not be applicable to all markers in the same scene.

B. Evaluation of Point Cloud Registration Accuracy

Data. Given that the existing point cloud registration benchmarks [6], [21], [22] lack fiducial markers in the scenes, we construct a new dataset, as shown in Fig. 8, with the Livox MID-40. As illustrated in the caption of Fig. 8, our dataset cover various indoor and outdoor scenes. Indoors, multiple 16.4 cm \times 16.4 cm AprilTags [10] are positioned in the environment. Outdoors, multiple 69.2 cm \times 69.2 cm ArUcos

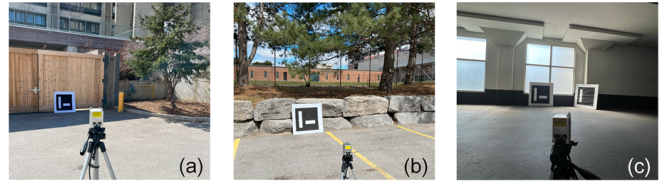


Fig. 7. Setup for testing the adaptive threshold marker detection algorithm: (a) between groups of buildings, (b) in open outdoor areas, and (c) in large indoor parking lots.

TABLE I
DEMONSTRATION OF THE NECESSITY OF THE PROPOSED ADAPTIVE MARKER DETECTION ALGORITHM

Scene	x (m)	y (m)	λ^*	Scene	x (m)	y (m)	λ^*	Scene	x (m)	y (m)	λ^*
Fig. 7(a)	0	4	36	Fig. 7(b)	0	4	7	Fig. 7(c)	4	4	20/6
	4	4	9		4	4	8		4	4	8/8
	-4	4	6		-4	4	6		-4	4	6/8
	0	5	20		0	5	9		0	5	15/10
	5	5	8		5	5	8		5	5	8/12
	-5	5	7		-5	5	9		-5	5	7/13
	0	6	19		0	6	9		0	6	8/13
	6	6	10		6	6	6		6	6	11/11
	-6	6	11		-6	6	8		-6	6	11/10
	0	7	17		0	7	9		0	7	19/20
	7	7	8		7	7	8		7	7	15/14
	-7	7	9		-7	7	9		-7	7	28/16
	0	8	15		0	8	13		0	8	10/16
	8	8	9		8	8	11		8	8	11/17
	-8	8	10		-8	8	15		-8	8	12/15
	0	9	17		0	9	10		0	9	13/11
	9	9	8		9	9	12		9	9	20/26
	-9	9	9		-9	9	12		-9	9	16/12
	0	10	14		0	10	13		0	10	24/28
	10	10	11		10	10	10		10	10	10/19
	-10	10	12		-10	10	15		-10	10	15/19

[11] are placed in the environment. Note that since the LiDAR fiducial markers in this work are thin sheets of objects attached to other surfaces, they are almost invisible in the point clouds. This is infeasible if we adopt LiDARTags [18] or calibration boards [15], [16], [17] to provide fiducials. These scenes are challenging due to low overlap, and the overlap rate [2] of each scene is presented in Table II. **Competitors and Metrics.** Competitors include the state-of-the-art (SOTA) learning-based multiview point cloud registration method, SGHR [1], and the SOTA pairwise geometry-based method, Teaser++ [3]. We employ the root-mean-square errors (RMSEs) [33] as the metric. We also compare the inference time of the methods with an AMD Ryzen 7 5800X CPU. **Results and Analysis.** The qualitative and quantitative results are presented in Fig. 8 and Table II, respectively. As seen, the proposed method yields the best accuracy and efficiency. SGHR [1] successfully registers the point clouds in scenes 1 to 3 while failing in scenes 4 to 10. Its efficiency is poor on the CPU, while the inference time is around 10s to 20s on an RTX 3090 GPU. Considering that Teaser++ [3] is a pairwise method, we manually select pairs of point clouds with overlap as the inputs (the same scheme adopted in the following tests), yet it still fails in all scenes. The failure cases show SGHR's limited generalization to unseen scenarios, and Teaser++ struggles with low overlap cases.

C. Application 1: 3D Asset Collection

An important application of point cloud registration is the 3D asset collection [34]. Thus, we evaluate the instance reconstruction quality of L-PR in this test. **Data.** The exper-

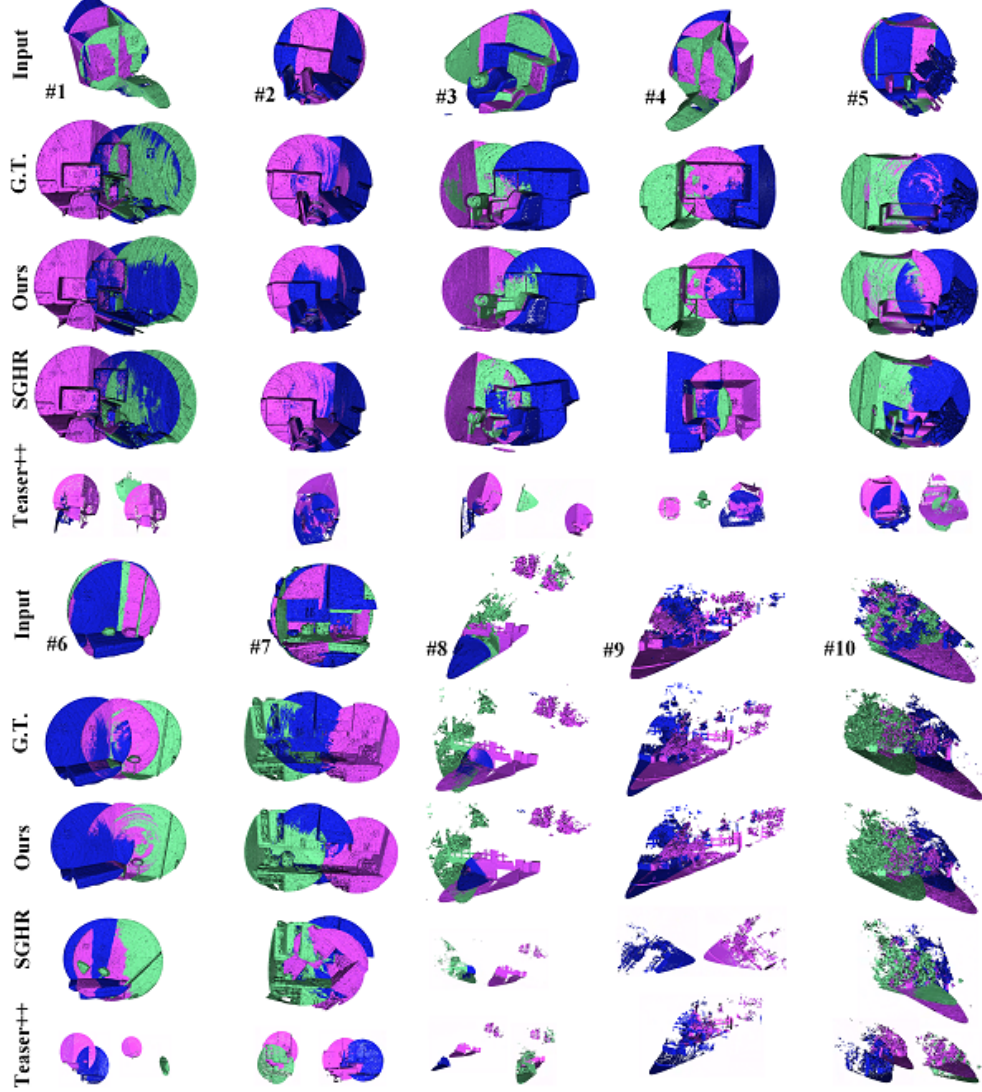


Fig. 8. Visual comparison with SOTAs (SGHR [1], Teaser++ [3]) on ten scenes. The scenes include the office (1-3), the meeting room (4), the lounge (5,6), the kitchen (7), the office building (8,9), and the thicket (10). Each scene consists of three scans, except scenes 2 and 9, which are composed of two scans.

perimental setup is depicted in Fig. 9. Four 69.2 cm \times 69.2 cm ArUco [11] markers are placed in the environment. We employ the Livox MID-40 LiDAR to scan the vehicle from five significantly different viewpoints. As shown in Fig. 9, this is also a challenging low-overlap case, with the average and minimum overlap rates being 13.39% and 1.02%, respectively. To evaluate the instance reconstruction quality, we use *Supervisely* [35], a popular 3D annotation tool, to extract the point cloud of the vehicle from the reconstruction result. Since the manufacture and model (Mercedes-Benz GLB) of the vehicle to be reconstructed are known, a high-fidelity 3D model acquired from a 3D assets website acts as the ground truth shape. **Metrics.** Following [34], we compute the Chamfer Distance and Recall between the ground truth shape and the reconstruction result. **Results and Analysis.** The qualitative result is shown in Fig. 9. As seen, SGHR is only able to align the third and fifth scans, while Teaser++ fails in all scenes even when pairs with overlap are manually selected and provided. By contrast, L-PR successfully aligns the unordered multiview point clouds and our reconstructed result preserves intricate

details. The Chamfer Distance and Recall of our reconstructed result are **0.003** and **96.22%**, respectively. This indicates [34] that L-PR can serve as a convenient tool for collecting high-fidelity 3D assets using the LiDAR sensor.

D. Application 2: Training Data Collection and Enhancement of Existing Learning-Based Method

Training data is crucial for learning-based methods. Most existing methods [1], [2] are trained on the 3DMatch dataset [6]. Augmenting the training data is beneficial for improving the generalization ability of learning-based methods. As demonstrated in Sections V-B and V-C, L-PR can automatically and efficiently register multiview low overlap 3D point clouds. Thus, it can serve as a valuable tool for collecting training data. In this section, we demonstrate that the training data collected using L-PR can enhance the performance of the SOTA method, SGHR [1], on various benchmarks, including 3DMatch [6], ETH [21], and ScanNet [22]. In particular, using L-PR, we process all the point clouds shown in Figs. 8 and 9, including 11 scenes with 33 scans, into the format required for

TABLE II
QUANTITATIVE COMPARISON WITH SGHR [1] AND TEASER++ [3] ON OUR DATASET

Scene #		1	2	3	4	5	6	7	8	9	10
Avg/Min Overlap Rate (%)		27.17/14.29	46.88/46.88	44.66/22.26	25.80/1.40	43.82/15.48	50.66/27.24	31.31/4.19	19.06/12.20	44.65/44.65	12.16/5.42
Teaser++[3]	RMSE _R (rad)	1.504	1.795	2.394	2.277	2.493	1.946	1.632	1.818	1.779	1.876
	RMSE _T (m)	1.724	1.890	2.075	2.252	1.911	1.733	2.089	1.861	1.848	1.891
	Time (s)	313.1	298.3	336.4	322.3	388.9	419.8	441.5	397.1	327.2	401.2
SGHR[1]	RMSE _R (rad)	0.152	0.060	1.198	1.825	1.311	1.696	4.42	2.792	3.034	2.810
	RMSE _T (m)	0.020	0.010	0.094	0.156	0.231	0.274	0.949	2.171	0.686	1.787
	Time (s)	846.1	785.0	886.5	825.3	851.7	979.3	983.6	909.9	794.6	950.4
Ours	RMSE _R (rad)	0.036	0.068	0.089	0.065	0.088	0.078	0.067	0.069	0.087	0.101
	RMSE _T (m)	0.017	0.011	0.028	0.031	0.032	0.043	0.019	0.082	0.069	0.077
	Time (s)	31.1	21.2	35.7	32.6	36.2	43.5	53.8	39.9	24.9	42.2

TABLE III
QUANTITATIVE EVALUATION OF THE ENHANCEMENT OF SGHR [1] DUE TO THE ADDITION OF LIVOX-3DMATCH TO THE TRAINING DATA.

Method	Dataset	RR \uparrow (%)	Dataset	RR \uparrow (%)	Dataset	RMSE _T (m) \downarrow Mean/Med	RMSE _R (deg) \downarrow Mean/Med
SGHR [1]	3DMatch [6]	92.68	ETH [21]	93.74	ScanNet [22]	0.66/0.51	23.50/22.08
SGHR [1] + Livox-3DMatch (our data)		95.58		98.03		0.51/0.45	20.87/17.21

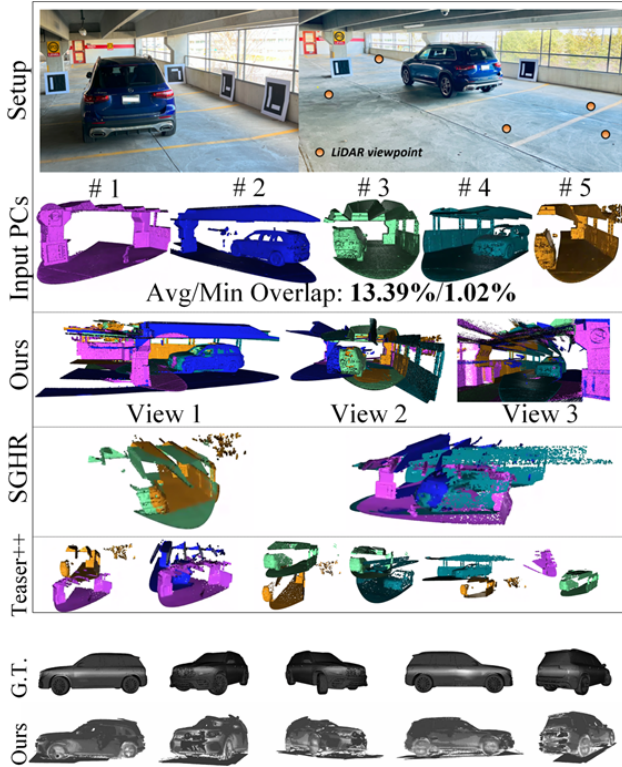


Fig. 9. An illustration of the experimental setup and a comparison of reconstruction results of Ours, SGHR [1], and Teaser++ [3].

training by SGHR. The newly collected data is named **Livox-3DMatch**. Then, we train SGHR from scratch using a mix of 3DMatch and Livox-3DMatch. In particular, the number of pairs in the training data increased from 14,400 to **17,700**, an increase of **22.91%**, thanks to the introduction of our data. Finally, we compare the performance of the SGHR models trained with only 3DMatch and with 3DMatch plus our data on popular benchmarks [6], [21], [22]. **Metrics.** Following [1], we use Registration Recall (RR) to evaluate performance on 3DMatch [6] and ETH [21], and RMSEs to report performance on ScanNet [22]. **Results and Analysis.** The quantitative results are presented in Table III. As seen, the RR of SGHR

is increased by **2.90%** on 3DMatch [6] and **4.29%** on ETH [21]. The translation error and rotation error on ScanNet [22] are decreased by **22.72%** and **11.19%**, respectively.

E. Application 3: Reconstructing a Degraded Scene

As previously introduced, the use of fiducial markers can enhance the robustness of reconstruction and localization in degraded scenes. Therefore, in this test, we evaluate our method in a textureless, degraded scene. **Data.** The setup is shown in the reference of Fig. 10. This scenario has repetitive structures and weak geometric features. We attach thirteen 16.4 cm \times 16.4 cm AprilTags to the wall. The LiDAR scans the scene from 11 viewpoints. We also captured 72 images with an iPhone 13 to use as input for SfM-M [14]. The ground truth trajectories are given by an OptiTrack Motion Capture system. **Competitors and Metrics.** Considering the competitors [1], [3] struggle in the degraded scene, we add SfM-M [14], the state-of-the-art marker-based SfM method, as a competitor. This addition enables a comprehensive and meaningful comparison. We employ the RMSEs as the metric. **Results and Analysis.** The qualitative results and trajectory comparison are presented in Fig. 10. Once again, SGHR and Teaser++ struggle in this scene. The quantitative results shown in Table IV demonstrate that the proposed approach achieves better localization accuracy, which is expected given that LiDAR is a ranging sensor.

TABLE IV
COMPARISON WITH SfM-M [14] REGARDING LOCALIZATION ACCURACY IN A DEGRADED SCENE.

Method \ Metric	RMSE _T (m) \downarrow	RMSE _R (rad) \downarrow
SfM-M [14]	0.0551	0.0491
Ours	0.0490	0.0384

F. Application 4: Localization in a GPS-denied Environment

Localization is also a crucial application of point cloud registration methods. Fiducial markers are a popular tool for providing localization information in GPS-denied environments, such as indoor parking lots. In this test, we compare the

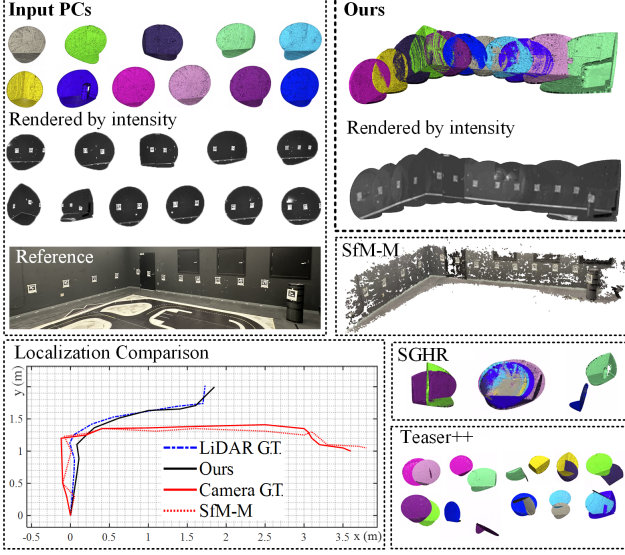


Fig. 10. Visualization of the scene reconstruction and localization results of different methods.

proposed method with KISS-ICP [4] in terms of localization accuracy. As shown in Fig. 11(a), four $69.2\text{ cm} \times 69.2\text{ cm}$ ArUco [11] markers are deployed in the environment. The vehicle, equipped with an RS-Ruby 128-beam mechanical LiDAR, follows an 8-shaped trajectory without pausing and samples 364 LiDAR scans. We conduct the experiment on the roof of a large parking lot to acquire the ground truth trajectory from the Real-Time Kinematic. However, our method is also applicable to indoor GPS-denied environments. As seen in Fig. 11(b) and Table V, our method exhibits less drift in the middle of the trajectory.

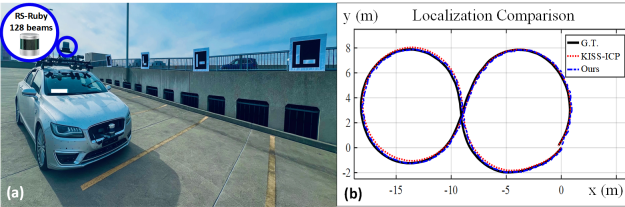


Fig. 11. (a): An illustration of the experimental setup. (b): Comparison of the trajectories given by different methods.

TABLE V
COMPARISON WITH KISS-ICP [4] REGARDING LOCALIZATION.

Method \ Metric	RMSE_T (m) \downarrow	RMSE_R (rad) \downarrow
KISS-ICP [4]	0.1976	0.1617
Ours	0.1715	0.1394

G. Application 5: 3D Map Merging

By cooperating with the algorithm introduced in [36], the proposed L-PR can be utilized for 3D map merging, as shown in Fig. 12. These 3D maps are extremely low overlap cases. In particular, the overlap rates [2] are 4.87% between map 1 and map 2, 3.96% between map 1 and map 3, and 2.59% between map 2 and map 3.

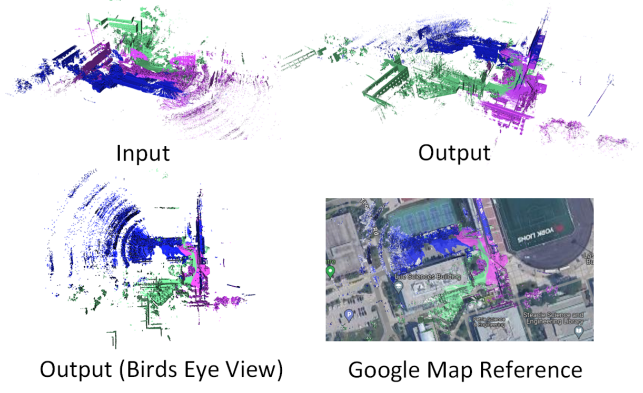


Fig. 12. An illustration of 3D map merging using L-PR.

VI. CONCLUSION

In this work, we develop L-PR, a novel framework that exploits LiDAR fiducial markers for unordered low overlap multiview point cloud registration. The markers in this work are thin sheets of paper attached to other surfaces, without impacting the 3D environment. L-PR consists of an adaptive threshold marker detection method and two levels of graphs. The adaptive threshold method robustly detects markers even when there are dramatic changes in viewpoints among scans, thus overcoming the limitation of [19]. The proposed two-level graph efficiently aligns the low overlap multiview point clouds directly from an unordered set by optimizing a MAP problem. We conduct qualitative and quantitative experiments to demonstrate the superiority of L-PR over previous SOTA methods and the diverse applications of L-PR, including 3D asset collection, training data collection, reconstruction of a degraded scene, localization in a GPS-denied environment, and 3D map merging. In particular, we collect a new training dataset named Livox-3DMatch using L-PR. The Livox-3DMatch dataset expands the original 3DMatch training data from 14,400 pairs to 17,700 pairs, representing a 22.91% increase. Training on this augmented dataset improves the performance of the SOTA learning-based method SGHR [1] by 2.90% on 3DMatch [6], 4.29% on ETH [21], and 22.72% (translation) / 11.19% (rotation) on ScanNet [22]. Future work includes utilizing L-PR to collect more 3D assets and point cloud registration training data to benefit the development of learning-based methods [34], [1].

REFERENCES

- [1] H. Wang, Y. Liu, Z. Dong, Y. Guo, Y.-S. Liu, W. Wang, and B. Yang, “Robust multiview point cloud registration with reliable pose graph initialization and history reweighting,” in *Proc. of the IEEE/CVF Conference on Computer Vision and Pattern Recognition*, 2023, pp. 9506–9515.
- [2] S. Huang, Z. Gojcic, M. Usvyatsov, A. Wieser, and K. Schindler, “Predator: Registration of 3d point clouds with low overlap,” in *Proc. of the IEEE/CVF Conference on Computer Vision and Pattern Recognition*, June 2021, pp. 4267–4276.
- [3] H. Yang, J. Shi, and L. Carlone, “Teaser: Fast and certifiable point cloud registration,” *IEEE Transactions on Robotics*, vol. 37, no. 2, pp. 314–333, 2020.
- [4] I. Vizzo, T. Guadagnino, B. Mersch, L. Wiesmann, J. Behley, and C. Stachniss, “KISS-ICP: In Defense of Point-to-Point ICP – Simple, Accurate, and Robust Registration If Done the Right Way,” *IEEE Robotics and Automation Letters*, vol. 8, no. 2, pp. 1029–1036, 2023.

[5] J. Lin and F. Zhang, "Loam livox: A fast, robust, high-precision lidar odometry and mapping package for lidars of small fov," in *Proc. IEEE International Conference on Robotics and Automation*, 2020, pp. 3126–3131.

[6] A. Zeng, S. Song, M. Nießner, M. Fisher, J. Xiao, and T. Funkhouser, "3dmatch: Learning local geometric descriptors from rgb-d reconstructions," in *Proc. of the IEEE conference on computer vision and pattern recognition*, 2017, pp. 1802–1811.

[7] Z. Gojcic, C. Zhou, J. D. Wegner, L. J. Guibas, and T. Birdal, "Learning multiview 3d point cloud registration," in *Proc. of the IEEE/CVF conference on computer vision and pattern recognition*, 2020, pp. 1759–1769.

[8] M. A. Fischler and R. C. Bolles, "Random sample consensus: a paradigm for model fitting with applications to image analysis and automated cartography," *Communications of the ACM*, vol. 24, no. 6, pp. 381–395, 1981.

[9] C. Yang, Z. Chai, X. Yang, H. Zhuang, and M. Yang, "Recognition of degradation scenarios for lidar slam applications," in *Proc. IEEE International Conference on Robotics and Biomimetics*. IEEE, 2022, pp. 1726–1731.

[10] M. Krogius, A. Haggemiller, and E. Olson, "Flexible layouts for fiducial tags," in *Proc. IEEE/RSJ International Conference on Intelligent Robots and Systems*, 2019, pp. 1898–1903.

[11] F. J. Romero-Ramirez, R. Muñoz-Salinas, and R. Medina-Carnicer, "Speeded up detection of squared fiducial markers," *Image and vision Computing*, vol. 76, pp. 38–47, 2018.

[12] R. Muñoz-Salinas, M. J. Marín-Jimenez, E. Yeguas-Bolívar, and R. Medina-Carnicer, "Mapping and localization from planar markers," *Pattern Recognition*, vol. 73, pp. 158–171, 2018.

[13] R. Muñoz-Salinas, M. J. Marín-Jimenez, and R. Medina-Carnicer, "Spm-slam: Simultaneous localization and mapping with squared planar markers," *Pattern Recognition*, vol. 86, pp. 156–171, 2019.

[14] Z. Jia, Y. Rao, H. Fan, and J. Dong, "An efficient visual sfm framework using planar markers," *IEEE Transactions on Instrumentation and Measurement*, vol. 72, pp. 1–12, 2023.

[15] J. Beltrán, C. Guindel, A. de la Escalera, and F. García, "Automatic extrinsic calibration method for lidar and camera sensor setups," *IEEE Transactions on Intelligent Transportation Systems*, vol. 23, no. 10, pp. 17 677–17 689, 2022.

[16] L. Tao, L. Pei, T. Li, D. Zou, Q. Wu, and S. Xia, "Cpi: Lidar-camera extrinsic calibration based on feature points with reflection intensity," in *Spatial Data and Intelligence: First International Conference, SpatialDI 2020, Virtual Event, May 8–9, 2020, Proceedings 1*. Springer, 2021, pp. 281–290.

[17] Y. Xie, L. Deng, T. Sun, Y. Fu, J. Li, X. Cui, H. Yin, S. Deng, J. Xiao, and B. Chen, "A4lidartag: Depth-based fiducial marker for extrinsic calibration of solid-state lidar and camera," *IEEE Robotics and Automation Letters*, vol. 7, no. 3, pp. 6487–6494, 2022.

[18] J.-K. Huang, S. Wang, M. Ghaffari, and J. W. Grizzle, "Lidartag: A real-time fiducial tag system for point clouds," *IEEE Robotics and Automation Letters*, vol. 6, no. 3, pp. 4875–4882, 2021.

[19] Y. Liu, H. Schofield, and J. Shan, "Intensity image-based lidar fiducial marker system," *IEEE Robotics and Automation Letters*, vol. 7, no. 3, pp. 6542–6549, 2022.

[20] J.-K. Huang and J. W. Grizzle, "Improvements to target-based 3d lidar to camera calibration," *IEEE Access*, vol. 8, pp. 134 101–134 110, 2020.

[21] F. Pomerleau, M. Liu, F. Colas, and R. Siegwart, "Challenging data sets for point cloud registration algorithms," *The International Journal of Robotics Research*, vol. 31, no. 14, pp. 1705–1711, 2012.

[22] A. Dai, A. X. Chang, M. Savva, M. Halber, T. Funkhouser, and M. Nießner, "Scannet: Richly-annotated 3d reconstructions of indoor scenes," in *Proceedings of the IEEE conference on computer vision and pattern recognition*, 2017, pp. 5828–5839.

[23] B. Pfrommer and K. Daniilidis, "Tagslam: Robust slam with fiducial markers," *arXiv preprint arXiv:1910.00679*, 2019.

[24] C. Li, Y. Ren, and B. Liu, "Pcgen: Point cloud generator for lidar simulation," in *Proc. IEEE International Conference on Robotics and Automation*. IEEE, 2023, pp. 11 676–11 682.

[25] B. Zhao, X. Chen, X. Le, J. Xi, and Z. Jia, "A comprehensive performance evaluation of 3-d transformation estimation techniques in point cloud registration," *IEEE Transactions on Instrumentation and Measurement*, vol. 70, pp. 1–14, 2021.

[26] Y. Wu, Q. Yao, X. Fan, M. Gong, W. Ma, and Q. Miao, "Panet: A point-attention based multi-scale feature fusion network for point cloud registration," *IEEE Transactions on Instrumentation and Measurement*, vol. 72, pp. 1–13, 2023.

[27] M. Khoury, Q.-Y. Zhou, and V. Koltun, "Learning compact geometric features," in *Proc. of the IEEE international conference on computer vision*, 2017, pp. 153–161.

[28] J. Nie, X. Lu, Z. Shen, and Y. Wang, "Singlereg: An unsupervised registration method for point cloud with good generalization performance," *IEEE Transactions on Instrumentation and Measurement*, 2024.

[29] T. D. Barfoot, *State estimation for robotics*. Cambridge University Press, 2017.

[30] E. W. Dijkstra, "A note on two problems in connexion with graphs," in *Edsger Wybe Dijkstra: His Life, Work, and Legacy*, 2022, pp. 287–290.

[31] M. Kaess, H. Johannsson, R. Roberts, V. Ila, J. Leonard, and F. Dellaert, "isam2: Incremental smoothing and mapping with fluid relinearization and incremental variable reordering," in *Proc. of IEEE International Conference on Robotics and Automation*, 2011, pp. 3281–3288.

[32] F. Dellaert and M. Kaess, *Factor Graphs for Robot Perception*. Foundations and Trends in Robotics, Vol. 6, 2017. [Online]. Available: <http://www.cs.cmu.edu/~kaess/pub/Dellaert17fnt.pdf>

[33] S. Zhang, J. Shan, and Y. Liu, "Variational bayesian estimator for mobile robot localization with unknown noise covariance," *IEEE/ASME Transactions on Mechatronics*, vol. 27, no. 4, pp. 2185–2193, 2022.

[34] S. Duggal, Z. Wang, W.-C. Ma, S. Manivasagam, J. Liang, S. Wang, and R. Urtasun, "Mending neural implicit modeling for 3d vehicle reconstruction in the wild," in *Proc. of the IEEE/CVF Winter Conference on Applications of Computer Vision*, 2022, pp. 1900–1909.

[35] Supervisely. Supervisely Computer Vision platform. (2023). [Online]. Available: <https://supervisely.com>

[36] Y. Liu, J. Shan, and H. Schofield, "Fiducial tag localization on a 3d lidar prior map," 2024. [Online]. Available: <https://arxiv.org/abs/2209.01072>



Yibo Liu (Student Member, IEEE) received the B.Sc. and M.Sc. degrees from Beihang University, Beijing, China, in 2017 and 2020, respectively. Since January 2020, he has been pursuing his Ph.D. degree in Earth and Space Science at York University, Toronto, Ontario, Canada. Since June 2022, he has been working as a part-time associate researcher at Huawei Noah's Ark Lab in Markham, Ontario, Canada. His research interests include Robot Vision and 3D Computer Vision.



Jinjun Shan (Senior Member, IEEE) received the Ph.D. degree in spacecraft design from the Harbin Institute of Technology, Harbin, China, in 2002. He is currently a Full Professor of Space Engineering at the Department of Earth and Space Science and Engineering, York University, Toronto, ON, Canada. His research interests include dynamics, control, and navigation. Dr. Shan is a Fellow of Canadian Academy of Engineering, a Fellow of Engineering Institute of Canada (EIC) and a Fellow of American Astronautical Society (AAS).



Amaldev Haridevan received his B.Eng degree from York University, Toronto, Ontario, Canada in 2021. He is now working towards a M.Sc. degree with the Department of Earth and Space Science and Engineering, York University, Toronto, Ontario, Canada. His research interests are in Robot Vision and Reinforcement Learning.



Shuo Zhang received the Ph.D. degree in precision instrument from Beihang University, Beijing, China, in 2016. He worked as a Postdoctoral Fellow with Tsinghua University, Beijing, China, from 2016 to 2019. He was a Postdoctoral Fellow with University of Alberta, Edmonton, AB, Canada, from 2019 to 2020. He is currently a Postdoctoral Fellow with the Department of Earth and Space Science and Engineering, York University, Toronto, ON, Canada. His research interests include optimal estimation, multi-sensor fusion, and navigation.